ENSO oscillatory regimes controlled by the zonal location of air-sea coupling region

BRANDON A. MOLINA* AND PEDRO N. DINEZIO

Atmospheric and Oceanic Sciences Department,

University of Colorado, Boulder, Colorado

CLARA DESER

National Center for Atmospheric Research, Boulder, Colorado

**Corresponding author*: Brandon A. Molina, brandon.molina@colorado.edu

ABSTRACT

The oscillatory dynamics of the El Niño-Southern Oscillation (ENSO) phenomenon are studied using numerical simulations performed with version 1 of the Community Earth System Model (CESM1). The CESM1 simulates the observed oscillatory regime characterized by El Niño events that consistently transition into La Niña and La Niña events that rarely transition into El Niño. Simulations of cold and warm climates show two distinct dynamical regimes associated with changes in these El Niño and La Niña transitions. In cold climates El Niño stop driving subsequent La Niña rendering ENSO completely non oscillatory. Conversely, in warm climates La Niña start driving subsequent El Niño making ENSO fully oscillatory. These changes are associated with zonal shifts in the region of strongly coupled winds and sea-surface temperature variations in the equatorial Pacific. This coupling region shifts eastward in warm climates. In this location the climatological thermocline is relatively shallow allowing thermocline variability driven by La Niña to positively feedback on the atmosphere favoring the onset of a subsequent El Niño. In contrast, the coupling region shifts westward in cold climates. The climatological thermocline is relatively deeper in this location preventing thermocline variability driven by El Niño to positively feedback on the atmosphere hindering the onset of a subsequent La Niña. This heightened sensitivity of ENSO oscillatory dynamics to the zonal location of the region of strong coupling reveals a potential for large changes in ENSO predictability in response to external forcings.

1. Introduction

The El Niño–Southern Oscillation (ENSO) phenomenon is typically thought as a self-sustained oscillation between its warm, El Niño phase and its cold, La Niña phase. Observed El Niño events regularly transition into La Niña consistent with the dynamics of an oscillation; however, La Niña events rarely drive a subsequent El Niño. Instead, La Niña conditions tend to persist for multiple years until the coupled ENSO system returns to a neutral state (Kessler 2002; Okumura and Deser 2010). The lack of a consistent La Niña to El Niño transition represents a breakdown of the oscillatory dynamics implicit in theoretical and conceptual models of ENSO (Suarez and Schopf 1988; Jin 1997). As a result, observed El Niño events are generally initiated by stochastic atmospheric variability with minimal influence from preceding La Niña via oscillatory dynamics (Timmermann et al. 2018).

Although the mechanisms underlying the onset, persistence, and decay of La Niña are well understood (Okumura et al. 2011; DiNezio and Deser 2014), the mechanisms whereby the oscillatory dynamics of El Niño and La Niña could change, particularly their temporal evolution, remain largely unexplored. Multi-model projections show an increase in the occurrence of 2-year La Niña under greenhouse warming (Geng et al. 2023) but it is unclear how this could affect the onset of subsequent El Niño. This is an important question because the lack of oscillatory dynamics underlying La Niña to El Niño transitions is a major cause of the limited predictability of El Niño relative to La Niña (Planton et al. 2018; Dommenget et al. 2012). Therefore exploring changes in ENSO oscillatory dynamics under altered climatic conditions could shed insights on mechanisms controlling the predictability of these highly disruptive climate phenomena.

The study of ENSO oscillatory regimes has been hindered by a lack of models that can simulate the observed asymmetry in the temporal evolution of El Niño and La Niña. Conceptual models of ENSO do not capture the observed asymmetries in event evolution because they represent El Niño and La Niña as part of a self-sustained oscillation in which warm and cold events follow each other regularly via delayed thermocline responses. These models propose that the transitions between ENSO phases are driven by a negative feedback involving delayed variations in the depth of the thermocline (Suarez and Schopf 1988; Jin 1997). This negative feedback operates with a delay, either due to the transit time of oceanic waves (Suarez and Schopf 1988), or due to the adjustment of the upper ocean to wind stress curl variations (Jin 1997). The adjustment times associated with these processes could change under altered climatic conditions. For instance, wave signals may have different travel times if they are forced at different locations along the equatorial Pacific or altered wind patterns could excite Rossby waves with different propagation speeds. According to the delayed oscillator theory, a shorter delay or wave transit time would lead to a non-oscillatory or stable mode where events grow and decay without reversing phase (Suarez and Schopf 1988). Conversely, ENSO could exhibit self-sustained oscillatory behavior if the wave transit time lengthens, allowing events more time to grow before being influenced by delayed thermocline responses. A meridionally broad wind stress pattern could excite slower Rossby waves, lengthening the transit time. However, these slower waves would be weaker, due to the weaker wind stress curl of a broader wind pattern. The weaker dynamic response would lead to a less effective upper ocean adjustment preventing a phase reversal; thus resulting in a non-oscillatory mode similar to the effect of a shorter delay. Therefore, a longer delay that maintains oscillatory behavior could only arise from increasing the distance between the western boundary and the coupling region (Kirtman et al. 1997; Neale et al. 2008). Moreover, conceptual models do not capture nonlinearities in feedback mechanisms responsible for the asymmetries in temporal evolution observed in nature (DiNezio and Deser 2014; Choi et al. 2013), thus limiting their use to study changes in oscillatory dynamics. Intermediate complexity models suffer from similar limitations despite including more physical processes. For instance, the Zebiak-Cane model, a fundamental dynamical framework for studying ENSO dynamics, does not represent the observed asymmetries in the evolution of El Niño and La Niña (Geng and Jin 2022), thus it is unclear if it can be used to study whether changes in climate can alter ENSO event transitions.

Coupled general circulation models simulate El Niño and La Niña transitions with increasing realism and could thus be used to study changes in ENSO oscillatory dynamics. One of the first models to exhibit these improvements was Version 4 of the Community Climate System Model (CCSM4) – a model capable of simulating irregular and hence realistic ENSO variability relative to previous versions of the model in which ENSO was regular due to excessive oscillatory behavior (Neale et al. 2008). The excessive oscillatory dynamics in previous versions of the model were mitigated thanks to improvements in the simulation of wind patterns. In CCSM4 and subsequent versions zonal wind anomalies are simulated with a broader, more realistic, meridional structure exciting slower Rossby waves (Deser et al. 2012). The slower and weaker oceanic responses produce more realistic asymmetries in the duration between El Niño and La Niña (Deser et al. 2012; DiNezio et al. 2017a; Capotondi et al. 2020). These advances in the simulation of the observed ENSO dynamics allow the study of changes under altered climate conditions.

Changes in the mean climate of the tropical Pacific could alter physical processes influencing ENSO oscillatory dynamics. The delay thermocline feedback governing ENSO event transitions (Suarez and Schopf 1988; Jin 1997) involves multiple physical processes that could change under altered climate conditions; amongst them, coupling between surface winds, thermocline depth, and sea-surface temperature (SST) variations (Timmermann et al. 2018; Capotondi et al. 2015). For instance, changes in the zonal extent of the western Pacific warm pool could affect how winds respond to SST variations by modulating the area along the equatorial Pacific favoring atmospheric convection (Picaut et al. 1996). Conversely, changes in upper ocean stratification could also affect how the thermocline responds to wind variability, but also the influence of thermocline variability on SST variations (Yeh et al. 2010). The delayed thermocline feedback can also be influenced by changes in the speed of off-equatorial Rossby waves affecting the time delay. This delay would become longer if waves were excited towards the eastern Pacific due to a larger distance travelled by the relatively slower Rossby waves.

Here we study mechanisms driving changes in ENSO oscillatory dynamics using simulations performed with version 1 of the Community Earth and System Model, a model that like its predecessor, CCSM4, can realistically simulate the observed oscillatory regime characterized by asymmetries in the temporal evolution of El Niño and La Niña. Our data consists of simulations of warmer and colder climate states representing past and future conditions together with a long simulation of pre-industrial (PI) climate used as control for evaluating the statistical significance of ENSO changes. First we describe the changes in the mean state and variability for SST and zonal wind stress in the tropical Pacific in each climate. Shifts in simulated patterns of variability motivated us to develop a technique to define a climate-specific coupling region to capture the location in the equatorial Pacific where the atmosphere is most responsive to oceanic variability. Our novel methodology reveals that this coupling region, currently associated with the Niño-3.4 region, shifts eastward in warmer climates and westward in colder climates. These shifts affect the coupling between wind, thermocline, and SST variations leading to changes in oscillatory behavior. Colder climates show a breakdown of the currently active El Niño to La Niña transition, while warmer climates show an activation of the currently inactive La Niña to El Niño transition – turning ENSO into a self-sustained oscillation. A heat budget analysis provides insight into the mechanisms whereby shifts in the coupling region modify the influence of delayed thermocline variations on the development of ENSO events under altered climate states.

2. Data and Methods

We analyzed output generated using the Community Earth System Model Version 1.2 (CESM1) – a coupled general circulation model consisting of the atmosphere, ocean, land, and cryosphere components, linked through a flux coupler (Hurrell et al. 2013). The CESM1 retains advances in the simulation of ENSO from its predecessor, CCSM4, with both versions simulating the observed asymmetries in the evolution of El Niño and La Niña events with high realism (Deser et al. 2012; DiNezio et al. 2017a). The atmospheric component is the Community Atmosphere Model Version 5 (CAM5), including new schemes for the simulation of moist turbulence, a shallow convection, cloud microphysics, and aerosol-cloud-rainfall interactions (Hurrell et al. 2013). In our simulations, CAM5 was configured on a finite volume grid at a nominal horizontal resolution of 2° with 30 pressure levels for the vertical coordinate. The land component is the Community Land Model Version 4 (CLM4) configured on the same horizontal grid as the atmosphere model. The ocean model is the Parallel Ocean Program Version 2 (POP2) configured at the nominal horizontal resolution of 1° with increased meridional resolution of about 1/3°approaching the equatorial wave guide, and 60 vertical levels. POP2 has parameterizations that simulate overflows, tidal mixing, and eddy mixing.

Our simulations span a range of externally forced changes in the mean climate state and variability in the tropical Pacific. Two simulations represent climate conditions under glacial conditions, one for the Last Glacial Maximum (LGM) 21,000 years before present (21 ka BP) and the other for an interval during the last deglaciation at 15 ka BP. These simulations were run with realistic ice sheets topography, coastlines, greenhouse concentrations, and insolation patterns following paleoclimate modeling protocols as described in Thirumalai et al. (2024). The 21 ka BP climate has orbital forcing closest to our current climate while the 15 ka BP has orbital forcing of precession that is substantially different from today leading to altered insolation affecting the annual cycle of the cold tongue – a well known driver of ENSO changes (Clement et al. 1999; Timmermann et al. 2007). Two additional simulations represent warmer climates under doubled and quadrupled atmospheric CO_2 concentrations relative to PI values (2xCO_2 and 4xCO_2). All four simulations were run until global mean surface temperature reached equilibrium. The analysis was performed on subsequent output from an equilibrated climate. We use 500 years of monthly output for the analysis, except for the 4xCO_2 simulation for which we use the last 300 years of near equilibrated climate (Table 1). All four simulations have a drift in global mean surface temperature less than 0.11 K per century during the analysis interval (Thirumalai et al. 2024). We compare variability in these simulations relative to a control simulation of PI climate. The length of this simulation, 1500 years, allows us to quantify unforced centennial variability under constant PI forcing. This was essential to assess whether the changes simulated under glacial and greenhouse conditions are forced. Note that our glacial and greenhouse warming simulations have a length well within the requirement to identify externally forced changes in ENSO in multi-century simulations (Wittenberg 2009). The 4xCO_2 simulation shows a very regular ENSO with reduced centennial variability allowing the use of only 300 years to detect changes relative to the PI control.

We used ocean and atmosphere variables from the CESM1 standard output to analyze ENSO dynamics and quantify physical processes. To capture the seasonal modulation of ENSO variability, all variables were analyzed at monthly temporal resolution. Anomalies were then calculated by removing the long-term monthly mean seasonal cycle from each year of the simulations. Finally, to isolate and focus on ENSO variability, monthly anomalies were smoothed with a bandpass filter spanning 6 months to 10 years. In addition to the standard CESM1 output, we also calculated the depth of the thermocline, defined as the depth at which the vertical temperature gradient is maximized, from 3-dimensional ocean model output. This calculation was restricted to the latitude band between 5°N and 5°S to represent the equatorial region. Unlike the typical definition based on the 20°C isotherm, using the depth of the maximum temperature gradient identifies the depth of the thermocline regardless of changes in ocean temperatures in each climate state (Vecchi and Soden 2007; DiNezio et al. 2009; Yang and Wang 2009). We also calculate the eastern edge of the western Pacific warm pool as the zero-contour of the atmospheric vertical velocity in pressure coordinates, ω, at the 500 hPa level, using the same latitude band (5°N–5°S). Unlike the definition based on the 28°C SST contour (De Deckker 2016), our definition of the warm pool edge is independent of the changes in SST in each climate state as it captures regions more prone to experience atmospheric convection. Locating the warm pool edge along the equatorial Pacific is important to identify the region where atmospheric convection will be most sensitive to changes in SST associated with ENSO.

To evaluate the realism of El Niño and La Niña transitions in our PI control simulation, we analyze observational SST and surface wind stress data. For SST, we use the NOAA Extended Reconstructed Sea Surface Temperature Version 5 (ERSSTv5) dataset (Huang et al. 2017), which spans 1854–2023 and provides a robust basis for estimating ENSO statistics and comparing them with our PI control simulation. Historical forcings have shown limited influence on ENSO variability (Maher et al. 2023), enabling meaningful comparisons between PI simulations and historical data. Surface wind stress data are drawn from the fifth-generation ECMWF atmospheric reanalysis (ERA5) (Hersbach et al. 2020). To account for long-term trends, both observational datasets have been quadratically detrended. By using SST and surface wind stress data from the common period of 1950–2023, we identify the coupling region under current climate conditions and assess the methodology for locating this region in the PI control simulation.

Definition of ENSO events

We define ENSO events using a novel Climate-Specific Niño (CSN) index that accounts for the shifting dynamics of the coupling region – the area with strongest air-sea interactions along the equatorial Pacific – across different climate states. Unlike the conventional Niño3.4 region, we use an adjusted region with zonally varying boundaries. The specific longitudinal bounds are detailed in Table 2, and the methodology for determining these adjustments is explained in Results section 2. To mitigate biases arising from varying ENSO amplitudes, we implement a standardized method for detecting El Niño and La Niña. We identify these events events when the CSN SST anomalies during the December-January-February (DJF) season exceed +1 or -1 standard deviation, respectively. This normalization technique ensures a consistent and unbiased detection of ENSO events across diverse climatic conditions. To provide a comprehensive understanding of ENSO's temporal evolution, we employ a systematic composite analysis methodology. By aligning the Decembers of all single-year and final year of multi-year events, we can focus on the transitions out of each ENSO phase. This methodology allows us to systematically track the evolution of ENSO events before, during, and after their peak, revealing the underlying mechanisms driving their initiation, growth, and decay. This approach provides a robust framework for analyzing El Niño and La Niña transitions across different climate states, ensuring consistent event detection and allowing us to explore the processes governing ENSO phase transitions.

Mixed Layer Heat Budget

We perform an upper ocean heat budget analysis following DiNezio and Deser (2014) in order to diagnose the physical processes involved in the transitions between El Niño and La Niña.

$$\rho_0 c_p H \frac{\partial [T']}{\partial t} = -\rho_0 c_p \int_{-H}^{0} \left(u' \frac{\partial \overline{T}}{\partial x} + w' \frac{\partial \overline{T}}{\partial z} + \overline{w} \frac{\partial T'}{\partial z} \right) \mathrm{d}z + Q'_{atm} + \epsilon \tag{1}$$

The heat budget equation (1) is computed as a balance between the heat storage rate within the upper ocean mixed layer (left hand side of equation 1) and the advective heat fluxes into the same layer as well as the net atmospheric heat flux (right hand side of equation 1). H represents the depth of the layer in the upper ocean over which the heat budget is computed. Our choice of H ensures that the anomalies of temperature averaged over the surface layer, $[T']$, effectively capture the magnitude of evolution of SST anomalies. Our approach to closing the heat budget for $[T']$ focuses on the three main thermal advection terms involved in ENSO dynamics: (1) anomalous horizontal advection of the mean temperature gradient ($\frac{\partial \overline{T}}{\partial x}$) by the anomalous zonal velocity (u'), $-u'\frac{\partial \overline{T}}{\partial x}$, a term associated with zonal ocean current variations; (2) anomalous vertical advection of mean temperature gradient ($\frac{\partial \overline{T}}{\partial z}$) by the anomalous vertical velocity (w'), $-w'\frac{\partial \overline{T}}{\partial z}$, a term associated with upwelling variations; and (3) anomalous vertical advection of anomalous temperature gradient ($\frac{\partial T'}{\partial z}$) by the mean vertical velocity ($\overline{w}$), $-\overline{w}\frac{\partial T'}{\partial z}$, a term associated with thermocline depth variations. In the results, we demonstrate how these three terms plus the anomalous net air-sea heat flux balance the $[T']$ temporal tendency. This allows us to use a composite heat budget for El Niño events to diagnose the processes explaining the oscillatory dynamics.

3. Results

a. Changes in the Pacific mean state and variability

Our simulations show a wide range of changes in the mean climate of the equatorial Pacific relative to the PI simulation that could affect the physical processes governing ENSO dynamics. The simulations of glacial climates, 21 ka BP and 15 ka BP, exhibit a pattern of enhanced equatorial cooling in the tropical Pacific, which we emphasize by removing the tropical mean SST changes (Fig.1a & 1b, shading). This pattern of cooling intensifies towards the eastern Pacific leading to a stronger zonal SST gradient along the equator together with stronger southeasterly trade winds and surface wind divergence along the equator (Fig. 1a-b, vectors). Conversely, the simulations under increased greenhouse forcing, 2xCO_2 and 4xCO_2, exhibit a pattern of enhanced equatorial warming that intensifies towards the eastern Pacific leading to a weaker zonal SST gradient along the equator (Fig. 1c-d, shading) and weaker southeasterly trade winds and surface wind divergence (Fig. 1c-d, vectors). These patterns of cooling and warming are part of well-known climate responses simulated by CMIP-class models in response to greenhouse forcing (Vecchi and Soden 2007; DiNezio et al. 2009; Li et al. 2016). In models, these responses arise as part of a coupled response to changes in the global Walker circulation, which weakens in response to warming and strengthens in response to cooling (Vecchi and Soden 2007; DiNezio et al. 2011). The associated changes in the winds in the equatorial Pacific drive characteristic ocean responses, mainly changes in upwelling and thermocline depth, that amplify the temperature response along the equator (DiNezio et al. 2009). The changes simulated across all climates are highly consistent with this mechanism therefore we focus the analysis on the influence of the changes in the mean climate on ENSO dynamics.

Each simulated climate exhibits distinctive patterns of SST and zonal wind stress variability along the equatorial Pacific. In the PI simulation, both SST and wind stress variability feature a single broad maximum in the equatorial central Pacific (Fig. 2b & 3b) closely matching the observed patterns (Fig. 2a & 3a). By contrast, colder climates display weaker variability in both SST and zonal wind stress, divided into two centers of action – one in the west and one farther east for SST (Fig. 2c-d) and one in the far west and another in the central basin for wind stress (Fig. 3c-d). The warmer climates, on the other hand, are characterized by stronger variability in both SST and wind stress extending across the equatorial Pacific, with maximum values in the eastern basin for SST and central basin for wind stress (Fig. 2e-f, Fig. 3e-f). These consistent shifts in SST and wind stress variability across climates are suggestive of zonal shifts in the region of strongest ocean-atmosphere coupling. Locating this area of strong coupling is important to define indices of ENSO variability and to study the physical processes influencing the temporal evolution of events. For instance, if we used the typical Niño-3.4 box for the glacial climates, that region would not fully capture the SST and wind stress variability present in the western equatorial Pacific. Conversely, for the warmer climates the conventional Niño-3.4 definition of coupling region will not capture the SST variability concentrated over the eastern side of the basin.

b. Defining ENSO coupling region for each climate state

Defining an ENSO coupling region in each climate state requires identifying the region where zonal wind stress and SST anomalies are maximally correlated. We achieve this by computing the leading Empirical Orthogonal Function (EOF1) of zonal wind stress variability across the equatorial Pacific (5°N-5°S, 140°E-80°W). Then we regressed SST anomalies on the normalized principal component (PC1) timeseries of zonal wind stress variability and defined the coupling region of ENSO coupling centered in the location of the maximum SST anomaly regression values. When we apply this approach to observations, the resulting coupling region coincides with the conventional definition based on the Niño3.4 region (Fig. 4a). The PI simulation shows a similar pattern of SST-wind stress co-variability as observed, with the strongest values centered in the Niño3.4 region – although with a stronger SST anomaly amplitude.

Our technique to identify the coupling region reveals pronounced zonal shifts under colder and warmer climates. The most pronounced shift occurs in the deglacial climate (15 ka BP), with a pattern of coupled wind-SST variability displaced westward by 50° of longitude relative to its location in the PI climate (Fig. 4d). The glacial simulation (21 ka BP) shows a less pronounced westward shift of 30° in longitude (Fig. 4c). The 4xCO_2 simulation shows the most pronounced eastward displacement, with a peak in the pattern of coupled variability shifted 20° to the east of its location in the PI simulation (Fig. 4f), while the 2xCO_2 simulation shows a comparable eastward shift of 15° (Fig. 4e). These shifts in the location of wind-SST co-variability align closely with the locations of SST variability maxima depicted in Fig. 2. In colder climates, the westward-shifted region of strong wind-SST coupling correspond only to the location of the western Pacific maxima (Fig. 2c-d), while it is not yet clear why the eastern Pacific maxima is not captured. Similarly, in warmer climates, the eastward-shifted region of strong wind-SST coupling is consistent with the strong SST variability concentrated in the eastern equatorial Pacific (Fig. 2e-f). This highlights the effectiveness of using EOF analysis to accurately capture the zonal shifts in ENSO coupling across our different climate states.

We quantify ENSO SST variability using the CSN index defined based on the coupling region in each climate state (see Methods, Definition of ENSO events). We define the coupling region in each climate state spanning 25° of longitude to the east and west of the location of maximal wind-SST co-variability identified before and 5°S-5°N in latitude (Table 2). Defining the Climate Specific Niño (CSN) SST index based on this region ensures that we capture SST variations in the region of maximum coupled variability in each climatic state. To examine how the temporal evolution and frequency characteristics of ENSO variability vary across different climate states, we compute the auto-correlation function (ACF) and the power spectral density (PSD) based on the CSN SST index (Fig. 5). We use the ACF to identify changes in the evolution of ENSO events and the PSD to identify peaks and compare their sharpness across climatic states. We also analyze the ACF and PSD based on PC1 of equatorial SST anomalies to verify that our results are robust to the definition of coupling region.

c. Metrics of oscillatory behavior

The ACF of the CSN index captures the aggregated evolution for both El Niño and La Niña events and should therefore be interpreted with caution, particularly when the evolution of these events is not symmetric as under current climate conditions. Nonetheless, this metric provides useful information on two limits. An ACF that decays to zero correlation without any zero crossing indicates that El Niño and La Niña events are uncorrelated, i.e. that events grow and decay without triggering a subsequent event of the opposite phase. In this case, ENSO would reside in a fully non-oscillatory regime. In contrast, ENSO is fully oscillatory if the ACF shows periodic peaks at a given lag. In this limit, the power spectrum is a delta function at the period of oscillation.

Because the real world ENSO is not a perfect oscillation, the observed lagged ACF shows qualities of both the oscillatory and the damped limits as described above (Fig. 5a & 5c, black curve). The significant negative ACF (-0.2) between 1 to 3 year lags reflects the tendency for El Niño to transition into La Niña events that can last multiple years. The simulated PI climate shows an ACF in striking agreement with observations (Fig. 5a & 5c, yellow curve). The decay of the negative ACF values together with the lack of a positive peak at longer lags reflects the breakdown of oscillatory behavior at the end of La Niña rarely triggering a subsequent El Niño. The absence of positive peaks at multi-year lags indicates that ENSO events lose the memory of past variability after La Niña returns to neutral. This is also reflected in the PSD of observed and PI climate showing a peak at 4 years suggesting a preferred periodicity. However, the broadness of the peak suggests ENSO is not purely oscillatory, just as inferred from the ACF. This is consistent with previous work confirming that CESM1 provides a realistic simulation of ENSO oscillatory dynamics (DiNezio et al. 2017b; Capotondi et al. 2020).

d. Changes in oscillatory behavior

Our simulations show pronounced changes in ENSO oscillatory behavior across the different climatic states. Under glacial conditions, the ACF based on the CSN index and PC1 show a very weak negative correlation at lags longer than one year revealing not just a lack of a transition from El Niño to La Niña, but also a transition to a long-lived, albeit weak, cold state. (Fig. 5a & 5c, blue & light blue curves). This is further reflected by the broader and redder power spectra that shows no significant period consistent with a lack of oscillatory behavior. (Fig. 5b & 5d, blue & light blue curves). These changes in ACF and PSD in the glacial climates represent a complete breakdown of ENSO oscillatory dynamics. Conversely, under greenhouse warming, the ACF, either based on the CSN index or the PC1, show a pronounced negative peak at about 2 years, followed by a weaker positive peak at lags between 3.5 and 4 years. These changes are consistent with: 1) a more consistent transition from El Niño to La Niña, and 2) the activation of a La Niña to El Niño transition (Fig. 5a & 5c, orange & red curves). The positive peak in ACF at multi-year lags indicates that the ENSO system retains significant memory of the previous states consistent with increasingly oscillatory behavior in the 2xCO2 and 4xCO2 climates. This is supported by the sharper peaks in the power spectra centered at 3.5 year periodicities (Fig. 5b & 5d, orange and red curves).

Another approach to exploring changes in ENSO oscillatory behavior is through the use of composites of ENSO events. The composite evolution of El Niño and La Niña events for each climate state, constructed using the CSN index as described in the methods section, illustrates these changes (Fig. 6). Unlike the ACF presented previously, these composites separately capture the temporal evolution and actual amplitudes of El Niño and La Niña phases. This separation provides a clearer understanding of the strength and progression of individual ENSO events across each climate. Additionally, the inclusion of probability density functions (PDFs) at key ENSO phases, reveals the distribution of individual events contributing to the composite mean. These PDFs indicate whether most events lean towards neutral, warm, or cold states during the transition period, revealing any changes in the oscillatory dynamics of ENSO in each climate state.

The composite analysis reveals significant differences in ENSO amplitude and transitions across climate states. Under glacial conditions, both El Niño and La Niña events tend to decay into neutral conditions without driving transitions to subsequent phases (Fig. 6a & 6c, blue and light blue curves). In the PI climate, the model realistically simulates El Niño consistently transitioning into La Niña, however, transitions from La Niña to El Niño are infrequent (Fig. 6a & 6c, black and yellow curves). In warmer climates, the transitions from El Niño to La Niña persist as seen in the PI climate, but transitions from La Niña to El Niño become more consistent. This indicates a shift towards a more self-sustained oscillatory behavior in warmer climates (Fig. 6a & 6c, orange and red curves).

e. Mechanisms underlying the changes in oscillatory dynamics

The heat budget analysis allows us to diagnose the processes involved in the changes in oscillatory behavior. Consistent with our earlier findings on SST variability, the glacial climates exhibit temperature anomalies, [T'], with smaller amplitudes (Fig. 7a, blue curve) compared to the PI climate, while warmer climates show temperature anomalies of comparable amplitude (Fig. 7b-c, blue curve). These magnitudes closely align with the rate of temperature change represented by the anomalous temperature tendency, $\frac{\partial [T']}{\partial t}$. For all climates, the evolution of $\frac{\partial [T']}{\partial t}$ (Fig. 7a-c, black curve) is primarily explained by a balance between the anomalous thermal advection terms (Fig. 7a-c, brown curve) and the anomalous net air-sea heat flux (Fig. 7a-c, yellow curve). Note that the anomalous thermal advective terms not included in the calculation of the full heat budget equation are incorporated into the residual term (Fig. 7a-c, magenta line). This residual term is either small in the colder climates or in phase with the total surface layer temperature tendency in the PI and $4xCO_2$ climates. This indicates that any unaccounted physical processes associated with the advective terms, included in the residual term, do not play a significant role in driving ENSO phase transitions. Accordingly, we focus our analysis on the zonal and vertical thermal advection terms, as they are directly in phase with the transition of ENSO events.

Zonal advection plays a role in driving El Niño events across different climatic conditions, acting as the primary mechanism in PI and glacial climates while becoming less important in the warmer climates. The composites of the anomalous zonal surface current (Fig. 7g-i, purple curve) and its associated anomalous zonal thermal advection (Fig. 7g-i, pink curve), reveal that this process is a significant driver of El Niño in the PI climate (Fig. 7h) and serves as the sole driver in glacial climates (Fig. 7g). Despite its crucial role in the PI climate and glacial periods, the anomalous zonal thermal advection does not exhibit significant changes in the warmer climates, particularly during the transition from La Niña to El Niño (Fig. 7i, Dec+2), suggesting a relative stability of this feedback mechanism across different climatic conditions. Therefore, to explore changes across climates, we focus on the anomalous vertical thermal advection term, $-\overline{w}\frac{\partial T'}{\partial z}$, since it is directly linked to thermocline depth variations involved in ENSO event transitions.

Under PI conditions, the location of the coupling region in the central Pacific (170°W-120°W) favors the onset of La Niña after El Niño and hinders the onset of El Niño after La Niña consistent with the evolution of observed events. The composite evolution of ENSO events shows that the equatorial thermocline shoals after the peak of El Niño (Fig. 7e, red curve), inducing a negative temperature tendency via the anomalous vertical thermal advection, $-\overline{w}\frac{\partial T'}{\partial z}$ (Fig. 7e, green curve). This cooling drives the demise of El Niño and the onset of a subsequent La Niña. Conversely, La Niña is followed by a deepening of the thermocline, producing a positive temperature tendency associated with the anomalous vertical thermal advection. However, this heating is weaker than the cooling that drives the onset of La Niña, making it insufficient to terminate La Niña and trigger a subsequent El Niño as shown by previous work using CCSM4 (DiNezio and Deser 2014), CESM1 (DiNezio et al. 2017b; Wu et al. 2021) and observations (Kessler 2002). This asymmetry in the magnitude of the thermocline-driven thermal advection explains the asymmetric evolution of El Niño and La Niña, consistent with previous work (DiNezio and Deser 2014).

In summary, our heat budget analysis shows that zonal shifts in the coupling region modify how delayed thermocline responses feedback on SSTs, leading to pronounced changes in El Niño and La Niña transitions. Ultimately these shifts explain the different ENSO oscillatory regimes simulated by our model across climatic states. Under glacial conditions, the transition from El Niño to La Niña shows a delayed shoaling of the thermocline, similar to what occurs under PI conditions. However, this anomalously deep thermocline generates a negligible cooling tendency via the anomalous vertical thermal advection (Fig. 7d, green curve). This muted cooling limits the ability of the system to fully transition to a subsequent La Niña. The breakdown of this transition makes El Niño and La Niña grow and decay in isolation, explaining the lack of memory of past ENSO events seen in the ACF and the lack of a clear spectral peak in SST anomalies. In warmer climates, in contrast, the deepening of the thermocline at Dec+3, driven by the peak of La Niña at Dec+2, generates a stronger heating tendency compared to PI conditions (Fig. 7f, green curve). This augmented heating more effectively terminates La Niña and triggers a subsequent El Niño, making ENSO oscillatory.

The simulations show changes in the depth the equatorial thermocline across climate states, with a deeper thermocline in the cold climates and a shallower thermocline in the warm climates (Fig. 8). The deeper climatological thermocline in the glacial states would inhibit the coupling between thermocline and SST variability. Conversely, coupling would be favored by the shallower climatological thermocline in the greenhouse climates. However, we do not find an intensification (or weakening) of the thermocline-driven anomalous vertical thermal advection, $-\overline{w}\frac{\partial T'}{\partial z}$, across climates when we average the terms of the heat budget over the fixed Niño3.4 region (not shown). This occurs because the deepening of the climatological thermocline in the colder climates is mirrored by a deepening of the climatological mixed layer (Fig. 8, blue curves). Conversely, the shoaling of the climatological thermocline in the warmer climates is mirrored by a shoaling of the climatological mixed layer (Fig. 8, red curves). In both cases the coupling between thermocline and SST variability, i.e. their distance, remains largely unchanged if we focus on a fixed region across the equatorial Pacific.

In contrast, the main control on ENSO event transitions is the location of the coupling region relative to the depth of the climatological thermocline. In the colder climates, the coupling region is located in the western equatorial Pacific where the climatological thermocline is deep. Conversely, in the warmer climates, the coupling region is located in the eastern equatorial Pacific where the climatological thermocline is shallow (Fig. 8). In the colder climates, thermocline variability produces muted thermal advection into the mixed layer because the thermocline variability during the onset of La Niña produces an anomalous thermal gradient, $\frac{\partial T'}{\partial z}$, located below the climatological mixed layer (Fig. 9b) relative to the PI climate (Fig. 9a). In other words, although the thermocline shoals after El Niño, the associated temperature fluctuations in the thermocline have a muted influence at the base of the mixed layer, explaining the negligible anomalous thermal advection, $-\overline{w}\frac{\partial T'}{\partial z}$, in the heat budget (Fig. 7d). In the warmer climates, thermocline variability during the onset of El Niño produces stronger thermal advection into the mixed layer because the thermocline variability produces an pronounced anomalous thermal gradient, $\frac{\partial T'}{\partial z}$, at the base of the climatological mixed layer (Fig. 9d) relative to the PI (Fig, 9c). In other words, in the warmer climates the coupling region is characterized by a shallower thermocline closer to the base of the mixed layer where thermocline variability can produce stronger anomalous thermal advection, $-\overline{w}\frac{\partial T'}{\partial z}$, as seen in the heat budget (Fig. 7f).

Our analysis shows that delayed thermocline responses are more effective at initiating ENSO events in climate states characterized by a coupling region co-located with a shallow climatological thermocline. Under glacial conditions, the thermocline deepens across the basin and the coupling region shifts westward where the mean thermocline is much deeper. Both effects decouple the thermocline from the surface preventing El Niño to drive a subsequent La Niña. In contrast, under warmer climates, the mean thermocline becomes shallower across the basin and the coupling region shifts eastward where the mean thermocline is much shallower. Both effects make delayed thermocline anomalies more effective at warming the surface during the decay of La Niña, facilitating the transition from La Niña to El Niño. These processes are clearly illustrated in the spatiotemporal evolution of composite events (Fig. 10), which demonstrates that thermocline anomalies can trigger subsequent events when the thermocline-induced SST anomalies occur within the ENSO's specific coupling region for the climate state.

The spatiotemporal evolution of composite events reveals that delayed thermocline responses generate SST anomalies, which can develop into El Niño or La Niña events depending on whether they occur in regions of strong ocean-atmosphere coupling in each climate state. Under glacial conditions, the shoaling of the thermocline following El Niño cools the ocean surface across much of the equatorial Pacific, driving its termination (Fig. 10a). However, the resulting negative SST anomalies occur too far east of the coupling region. This spatial offset, combined with the weak ocean-atmosphere coupling in that region, prevents the anomalies from amplifying into a subsequent La Niña like in the PI climate (Fig. 10b). In contrast, under warmer conditions, the deepening of the thermocline after the peak of La Niña generates a warming tendency within the coupling region specific to that climate (Fig. 10c). This allows the positive SST anomalies to grow and trigger a subsequent El Niño. These results highlight the critical role of the location of the coupling region in determining the effectiveness of thermocline variations in driving ENSO phase transitions across different climate states.

4. Discussion

Our analysis shows that ENSO oscillatory regimes are controlled by the location of the air-sea coupling region along the equatorial Pacific. Under current and PI conditions this region is located in the central equatorial Pacific coinciding with the Niño-3.4 region. This location hinders the onset of El Niño, driven by delayed thermocline responses associated with a preceding La Niña, explaining one of the more conspicuous asymmetries of the ENSO phenomenon. When the thermocline deepens after La Niña it cannot initiate a subsequent El Niño because the deep climatological thermocline in the central equatorial Pacific limits the magnitude of warming at the ocean surface needed to initiate a subsequent El Niño (DiNezio and Deser 2014). This can be seen in Fig. 10b of our analysis where the thermocline deepening associated with La Niña produces warming in the far eastern equatorial Pacific where the atmosphere is not responsive. The delayed thermocline responses driven by La Niña do not produce warming in the central equatorial Pacific, where the atmosphere is responsive to SSTs, because the anomalously deep thermocline becomes decoupled from the mixed layer. In contrast, El Niño events can consistently trigger subsequent La Niña because their associated thermocline shoaling can effectively drive cooling in the central Pacific where the atmosphere is response to SSTs. These ideas, originally proposed by DiNezio and Deser (2014), are supported by recent work showing that heat content, a proxy for thermocline depth, is a much better predictor of La Niña than of El Niño (Xue and Kumar 2017; Planton et al. 2018).

Thermocline variability associated with La Niña can drive subsequent El Niño when the coupling region shifts eastward. Under greenhouse warming, enhanced equatorial warming makes atmospheric convection and winds more responsive to SST anomalies towards the eastern equatorial Pacific, allowing thermocline variability to start playing a bigger role in the growth of El Niño events. Otherwise, under current conditions, cold and dry background conditions in this region make winds unresponsive to positive SST anomalies, thus limiting the influence of thermocline-induced warming on the initiation of El Niño. An eastward shift in the coupling region also makes the coupling between the thermocline and SSTs more effective due to the shallow climatological thermocline. This shift makes transitions more consistent, contributing to ENSO's transition towards a self-sustained oscillation. Conversely, when the coupling region shifts westward, as in our glacial simulations, the deep climatological thermocline reduces the coupling between thermocline variability and SSTs, preventing the growth of La Niña. In this regime, El Niño and La Niña occur in isolation without influence from previous events via thermocline dynamics. As a result of the westward shifted coupling region, the growth of ENSO events is likely to be dominated by stochastic atmospheric variability amplified by the zonal advection feedback at the edge of the warm pool as seen in our heat budget analysis.

Our heat budget analysis reveals large changes in the balance of zonal and vertical thermal advection processes during the onset of El Niño. As discussed above, an eastward shift of the ENSO coupling region makes the delayed thermocline feedback stronger, favoring oscillatory dynamics. However, the eastward shift also strengthens the thermal advection by zonal current anomalies (Fig. 7i) – the main physical process involved in the Bjerknes feedback during the growth of El Niño events (McPhaden and Yu 1999; Thirumalai et al. 2024). We attribute this change to the eastward shift in the coupling region too. The shallower climatological mixed layer over the eastern equatorial Pacific could make zonal currents more responsive to winds allowing a faster expansion of warm pool waters via zonal advective processes. A stronger zonal advection feedback could also favor the onset of El Niño events via stochastic wind variability in addition to a stronger influence from preceding La Niña via thermocline dynamics. This is particularly important for understanding future changes in ENSO variability. Virtually all previous studies of ENSO changes use the the Niño-3.4 region (170°W-120°W) to quantify ENSO variability (e.g., McPhaden et al. 2006; Vecchi and Wittenberg 2010; Timmermann et al. 1999). Our results, particularly the heat budget analysis, suggests that using a fixed region would conflate mechanisms driving changes in amplitude or frequency of ENSO events. We propose that the use of climate specific coupling regions is needed to study the impact of changes in mean climate on all aspects of ENSO variability, not only oscillatory dynamics.

The impact of zonal shifts in the coupling region could also be relevant for understanding ENSO flavors. As El Niño events grow, they are initially driven mostly by zonal advection at the edge of the warm pool where SST anomalies can feedback on the atmosphere McPhaden and Yu (1999). As events grow in magnitude, the atmosphere becomes more responsive to SSTs towards the eastern side of the basin. This shift in the region of coupling can excite the much stronger thermocline feedback in the eastern equatorial Pacific. This is consistent with previous work showing that spatial shifting of the Walker circulation controls ENSO complexity through the increased involvement of processes such as the ocean adjustment to wind stress (Thual and Dewitte 2023) or thermocline feedback (Capotondi 2013).

Although our results are based on a model that simulates a much more realistic ENSO temporal evolution than most other models, CESM1 still simulates too many high-amplitude east Pacific El Niño events. This bias could make ENSO appear more oscillatory, as these events are more prone to transitioning back into El Niño conditions, contrary to what is observed in reality. This does not unduly affect our results given that these events are relatively rare in the PI simulation, as shown by the realistic behavior of the ACF. However, further research should apply our method to simulations performed with other climate models with realistic ENSO evolution to assess the robustness of our results. Another important aspect to consider is that the altered climates used in our analysis are equilibrated relative to a constant forcing, unlike our current climate which is changing in response to transient forcings that include not only greenhouse gases, but also anthropogenic aerosols, stratospheric ozone change, and other forcing agents. Therefore it is unclear if the projected shift to a fully oscillatory regime will occur under continued emissions of CO_2. Finally, one key feature that requires further investigation is the presence of the two maxima in SST and zonal wind stress variance under glacial conditions (Figs. 2c,d; 3c,d). While the western maximum is linked to the leading mode of variability (PC1), the mechanisms driving the distinct eastern maximum remain unclear. Future studies should focus on understanding this eastern maximum, potentially through targeted model experiments to isolate the underlying physical processes.

Ultimately, our analysis reveals that shifts in the coupling region are dependent on the mean state change, and it is unclear whether simulated enhanced equatorial warming and associated weakening of the Walker circulation under ongoing greenhouse warming will materialize, especially given the lack of observational evidence (Wills et al. 2022). If instead, greenhouse warming produces a strengthening of the zonal SST gradient and equatorial easterly winds, as in the glacial climate state simulations, we would expect a westward shift in the coupling region and thus a less oscillatory ENSO. However, paleoclimatic evidence from the Pliocene, the most recent geological interval with CO_2 levels comparable to our idealized $2xCO_2$ scenario, indicates a weakened east-west gradient across the Pacific and a weaker Walker Circulation (Tierney et al. 2019). This evidence supports the crucial aspect of increased greenhouse warming effect on the Pacific mean state in our model predictions.

5. Conclusion

Our simulations demonstrate that El Niño-La Niña transitions and the associated dynamical regimes can experience pronounced changes under altered climatic states. Under global warming, the transition from La Niña to El Niño becomes more consistent, transforming ENSO into a more regular and predictable oscillation. In today's climate, this transition does not happen consistently because the delayed thermocline responses associated with La Niña cannot induce a subsequent El Niño. The thermocline deepening driven by La Niña drives anomalous heating in the central equatorial Pacific, which terminates La Niña; however, as the thermocline deepens, it decouples from the surface, limiting its ability to drive a subsequent El Niño (DiNezio and Deser 2014). This nonlinearity is less pronounced over the eastern equatorial Pacific, where the mean thermocline is sufficiently shallow that it never fully decouples from the surface layer even when it deepens, and thus continues to be effective at influencing SSTs. However, this is a region where the atmosphere is not responsive to SST variations because the mean conditions are too cold. However, the atmosphere becomes more responsive to SST variability in this region. This eastward shift in the region of strong coupling produces more regular transitions from La Niña to El Niño because the deepening of the thermocline following La Niña induces SST anomalies in the eastern Pacific that can grow via the Bjerknes feedback. This allows for the termination of La Niña to be followed by a subsequent El Niño, sustaining the ENSO cycle. Conversely, under colder climates, the coupling region of ENSO shifts to the western equatorial Pacific where the climatological thermocline is deep and thus the delayed thermocline shoaling following El Niño cannot produce SST anomalies capable of growing via the Bjerknes feedback. Together these results indicate that ENSO oscillatory behavior is highly sensitive to changes in mean climate, with potential implications for the predictability of El Niño under greenhouse warming.

Acknowledgments. BRM and PDN were supported by grant AGS-2103007. CD was supported by the National Science Foundation - National Center for Atmospheric Research.

References

Capotondi, A., 2013: ENSO diversity in the NCAR CCSM4 climate model. *Journal of Geophysical Research: Oceans*, **118 (10)**, 4755–4770, doi:10.1002/jgrc.20335.

Capotondi, A., C. Deser, A. S. Phillips, Y. Okumura, and S. M. Larson, 2020: ENSO and Pacific Decadal Variability in the Community Earth System Model Version 2. *J. Advances in Modeling Earth Systems*, **12 (12)**, e2019MS002 022, doi:10.1029/2019MS002022.

Capotondi, A., and Coauthors, 2015: Understanding ENSO Diversity. *Bull. Amer. Meteor. Soc.*, **96 (6)**, 921–938, doi:10.1175/BAMS-D-13-00117.1.

Choi, K., G. A. Vecchi, and A. T. Wittenberg, 2013: ENSO Transition, Duration, and Amplitude Asymmetries: Role of the Nonlinear Wind Stress Coupling in a Conceptual Model. *J. Climate*, **26 (23)**, 9462–9476, doi:10.1175/JCLI-D-13-00045.1.

Clement, A. C., R. Seager, and M. A. Cane, 1999: Orbital controls on the El Niño/Southern Oscillation and the tropical climate. *Paleoceanography*, **14 (4)**, 441–456, doi:10.1029/1999PA900013.

De Deckker, P., 2016: The Indo-Pacific Warm Pool: critical to world oceanography and world climate. *Geosci. Lett.*, **3 (20)**, doi:10.1186/s40562-016-0054-3.

Deser, C., and Coauthors, 2012: ENSO and Pacific Decadal Variability in the Community Climate System Model Version 4. *J. Climate*, **25 (8)**, 2622–2651, doi:10.1175/JCLI-D-11-00301.1.

DiNezio, P. N., A. Clement, G. A. Vecchi, B. Soden, A. J. Broccoli, B. L. Otto-Bliesner, and P. Braconnot, 2011: The response of the Walker circulation to Last Glacial Maximum forcing: Implications for detection in proxies. *Paleoceanography*, **26**, PA3217, doi:10.1029/2010PA002083.

DiNezio, P. N., A. C. Clement, G. A. Vecchi, B. J. Soden, B. P. Kirtman, and S. Lee, 2009: Climate Response of the Equatorial Pacific to Global Warming. *J. of Climate*, **22 (18)**, 4873–4892, doi:10.1175/2009JCLI2982.1.

DiNezio, P. N., and C. Deser, 2014: Nonlinear Controls on the Persistence of La Niña. *J. Climate*, **27 (19)**, 7335–7355, doi:10.1175/JCLI-D-14-00033.1.

DiNezio, P. N., C. Deser, A. Karspeck, S. Yeager, Y. Okumura, G. Danabasoglu, and G. A. Meehl, 2017a: A 2 year forecast for a 60–80% chance of La Niña in 2017–2018. *Geophys. Res. Lett.*, **44**, 11,624–11,635, doi:10.1002/2017GL074904.

DiNezio, P. N., C. Deser, Y. Okumura, and A. Karspeck, 2017b: Predictability of 2-year La Niña events in a coupled general circulation model. *Climate Dyn.*, **49**, 4237–4261, doi:10.1007/s00382-017-3575-3.

Dommenget, D., T. Bayr, and C. Frauen, 2012: Analysis of the non-linearity in the pattern and time evolution of El Niño-Southern Oscillation. *Climate Dyn.*, **40**, 2825–2847, doi:10.1007/s00382-012-1475-0.

Geng, L., and F.-F. Jin, 2022: ENSO Diversity Simulated in a Revised Cane-Zebiak Model. *Frontiers in Earth Science*, **10**, doi:10.3389/feart.2022.899323.

Geng, T., F. Jia, W. Cai, L. Wu, B. Gan, Z. Jing, S. Li, and M. J. McPhaden, 2023: Increased occurrences of consecutive La Niña events under global warming. *Nature*, **619 (7971)**, 774–781, doi:10.1038/s41586-023-06236-9.

Hersbach, H., and Coauthors, 2020: The ERA5 global reanalysis. *Q J R Meteorol Soc.*, **146 (730)**, 1999–2049, doi:10.1002/qj.3803.

Huang, B., and Coauthors, 2017: Extended Reconstructed Sea Surface Temperature, Version 5 (ERSSTv5): Upgrades, Validations, and Intercomparisons. *J. Climate*, **30 (20)**, 8179–8205, doi:10.1175/JCLI-D-16-0836.1.

Hurrell, J. W., and Coauthors, 2013: The Community Earth System Model: A Framework for Collaborative Research. *Bulletin of the American Meteorological Society*, **94 (9)**, 1339–1360, doi:10.1175/BAMS-D-12-00121.1.

Jin, F., 1997: An Equatorial Ocean Recharge Paradigm for ENSO. Part I: Conceptual Model. *J. Atmos. Sci.*, **54 (7)**, 811–829, doi:10.1175/1520-0469(1997)0542.0.CO;2.

Kessler, W. S., 2002: Is ENSO a cycle or a series of events? *Geophys. Res. Lett.*, **29 (23)**, 40–1–40–4, doi:10.1029/2002GL015924.

Kirtman, B. P., J. Shukla, B. Huang, Z. Zhu, and E. K. Schneider, 1997: Multiseasonal Predictions with a Coupled Tropical Ocean–Global Atmosphere System. *Monthly Weather Review*, **125 (5)**, 789–808, doi:10.1175/1520-0493(1997)125⟨0789:MPWACT⟩2.0.CO;2.

Li, G., S. P. Xie, Y. Du, and Y. Luo, 2016: Effects of excessive equatorial cold tongue bias on the projections of tropical Pacific climate change. Part I: The warming pattern in CMIP5 multi-model ensemble. *Climate Dyn.*, **47**, 3817–3831, doi:10.1007/s00382-016-3043-5.

Maher, N., and Coauthors, 2023: The future of the El Niño–Southern Oscillation: using large ensembles to illuminate time-varying responses and inter-model differences. *Earth System Dynamics*, **14 (2)**, 413–431, doi:10.5194/esd-14-413-2023.

McPhaden, M. J., and X. Yu, 1999: Equatorial waves and the 1997–98 El Niño. *Geophys. Res. Lett.*, **26 (19)**, 2961–2964, doi:10.1029/1999GL004901.

McPhaden, M. J., S. E. Zebiak, and M. H. Glantz, 2006: ENSO as an Integrating Concept in Earth Science. *Science*, **314 (5806)**, 1740–1745, doi:10.1126/science.1132588.

Neale, R. B., J. H. Richter, and M. Jochum, 2008: The Impact of Convection on ENSO: From a Delayed Oscillator to a Series of Events. *J. Climate*, **21 (22)**, 5904–5924, doi:10.1175/2008JCLI2244.1.

Okumura, Y. M., and C. Deser, 2010: Asymmetry in the Duration of El Niño and La Niña. *J. Climate*, **23 (21)**, 5826–5843, doi:10.1175/2010JCLI3592.1.

Okumura, Y. M., M. Ohba, C. Deser, and H. Ueda, 2011: A Proposed Mechanism for the Asymmetric Duration of El Niño and La Niña. *J. Climate*, **24 (15)**, 3822–3829, doi:10.1175/2011JCLI3999.1.

Picaut, J., M. Ioualalen, C. Menkes, T. Delcroix, and M. J. McPhaden, 1996: Mechanism of the Zonal Displacements of the Pacific Warm Pool: Implications for ENSO. *Science*, **274**, 1486–1489, doi:10.1126/science.274.5292.1486.

Planton, Y., J. Vialard, E. Guilyardi, M. Lengaigne, and T. Izumo, 2018: Western Pacific oceanic heat content: A better predictor of La Niña than of El Niño. *Geophys. Res. Lett.*, **45**, 9824–9833, doi:10.1029/2018GL079341.

Suarez, M. J., and P. S. Schopf, 1988: A Delayed Action Oscillator for ENSO. *J. Atmos. Sci.*, **45 (21)**, 3283–3287, doi:10.1175/1520-0469(1988)0452.0.CO;2.

Thirumalai, K., P. N. DiNezio, Y. Okumura, J. Partin, Liu, K. Costa, and A. Jacobel, 2024: Future increase in extreme El Niño supported by past glacial changes. *Nature*, **634**, 374–380, doi:10.1038/s41586-024-07984-y.

Thual, S., and B. Dewitte, 2023: ENSO complexity controlled by zonal shifts in the Walker circulation. *Nature Geoscience*, **16 (4)**, 328–332, doi:10.1038/s41561-023-01154-x.

Tierney, J. E., A. M. Haywood, R. Feng, T. Bhattacharya, and B. L. Otto-Bliesner, 2019: Pliocene warmth consistent with greenhouse gas forcing. *Geophys. Res. Lett.*, **46**, 9136–9144, doi:10.1029/2019GL083802.

Timmermann, A., S. I. An, J. S. Kug, and Coauthors, 2018: El Niño-Southern Oscillation Complexity. *Nature*, **559**, 535–545, doi:10.1038/s41586-018-0252-6.

Timmermann, A., A. Bacher, M. Esch, M. Latif, and E. Roeckner, 1999: Increased El Niño frequency in a climate model forced by future greenhouse warming. *Nature*, 694–697, doi:10.1038/19505.

Timmermann, A., S. J. Lorenz, S.-I. An, A. Clement, and S.-P. Xie, 2007: The Effect of Orbital Forcing on the Mean Climate and Variability of the Tropical Pacific. *Journal of Climate*, **20 (16)**, 4147 – 4159, doi:10.1175/JCLI4240.1.

Vecchi, G. A., and B. J. Soden, 2007: Global Warming and the Weakening of the Tropical Circulation. *J. Climate*, **20 (17)**, 4316–4340, doi:10.1175/JCLI4258.1.

Vecchi, G. A., and A. T. Wittenberg, 2010: El niño and our future climate: where do we stand? *WIREs Climate Change*, **1 (2)**, 260–270, doi:10.1002/wcc.33.

Wills, R. C. J., Y. Dong, C. Proistosecu, K. C. Armour, and D. S. Battisti, 2022: Systematic climate model biases in the large-scale patterns of recent sea-surface temperature and sea-level pressure change. *Geophys. Res. Lett.*, **49 (17)**, e2022GL100 011, doi:10.1029/2022GL100011.

Wittenberg, A. T., 2009: Are historical records sufficient to constrain ENSO simulations? *Geophys. Res. Lett.*, **36 (12)**, doi:10.1029/2009GL038710.

Wu, X., Y. M. Okumura, C. Deser, and P. N. DiNezio, 2021: Two-Year Dynamical Predictions of ENSO Event Duration during 1954–2015. *J. Climate*, **34 (10)**, 4069–4087, doi:10.1175/JCLI-D-20-0619.1.

Xue, Y., and A. Kumar, 2017: Evolution of the 2015/16 El Niño and historical perspective since 1979. *Sci. China Earth Sci.*, **60 (9)**, 1572–1588, doi:10.1007/s11430-016-0106-9.

Yang, H., and F. Wang, 2009: Revisiting the Thermocline Depth in the Equatorial Pacific. *J. Climate*, **22 (13)**, 3856–3863, doi:10.1175/2009JCLI2836.1.

Yeh, S. W., B. Dewitte, B. Y. Yim, and Y. Noh, 2010: Role of the upper ocean structure in the response of ENSO-like SST variability to global warming. *Climate Dyn.*, **35**, 355–369, doi:10.1007/s00382-010-0849-4.

LIST OF TABLES

TABLE 1: Boundary conditions of the simulated climates by CESM1.

Simulation	Atmospheric CO_2 (ppm)	Simulation Length (Yrs)
$4xCO_2$	1120	300
$2xCO_2$	560	500
0ka (PI)	280	1500
15ka	230	500
21ka	190	500

Table 2: Coupling region to compute ENSO variability

Simulation	Longitude Bounds
$4xCO_2$	145°W - 95°W
$2xCO_2$	150°W - 100°W
0ka (PI)	170°W - 120°W
15ka	145°E - 165°W
21ka	165°E - 145°W

LIST OF FIGURES

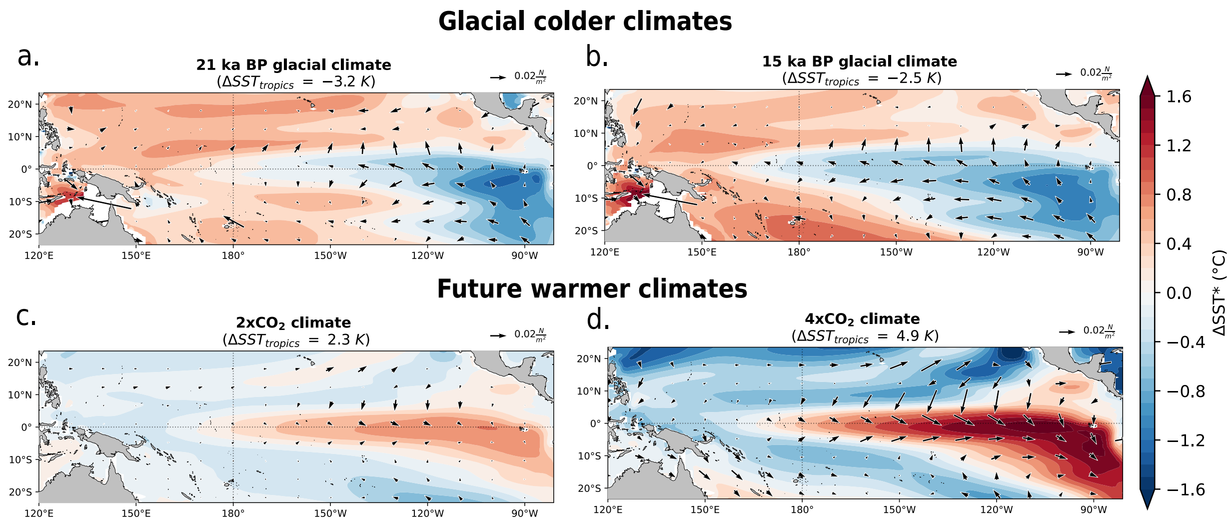

FIG. 1: **Simulated changes in the ocean surface mean state in altered climate states.**

Annual mean changes in relative sea-surface temperature (shading), surface wind stress (vectors), and thermocline depth (contours) simulated by the Community Earth System Model Version 1 (CESM1) under altered climatic conditions. Changes for colder climates (top) correspond to equilibrated responses to boundary conditions for glacial intervals 21 and 15 thousand years before present (21ka and 15ka simulation). Changes for warmer climates (bottom) correspond to equilibrated responses to increased greenhouse gas states under doubling and quadrupling of atmospheric CO_2 concentrations ($2xCO_2$ and $4xCO_2$ simulations respectively). Relative SST is defined as the departure from the tropical mean SST (20°N-20°S average) in each climate state. Changes in all variables are computed relative to a simulation of pre-industrial (PI) climate as described in Methods.

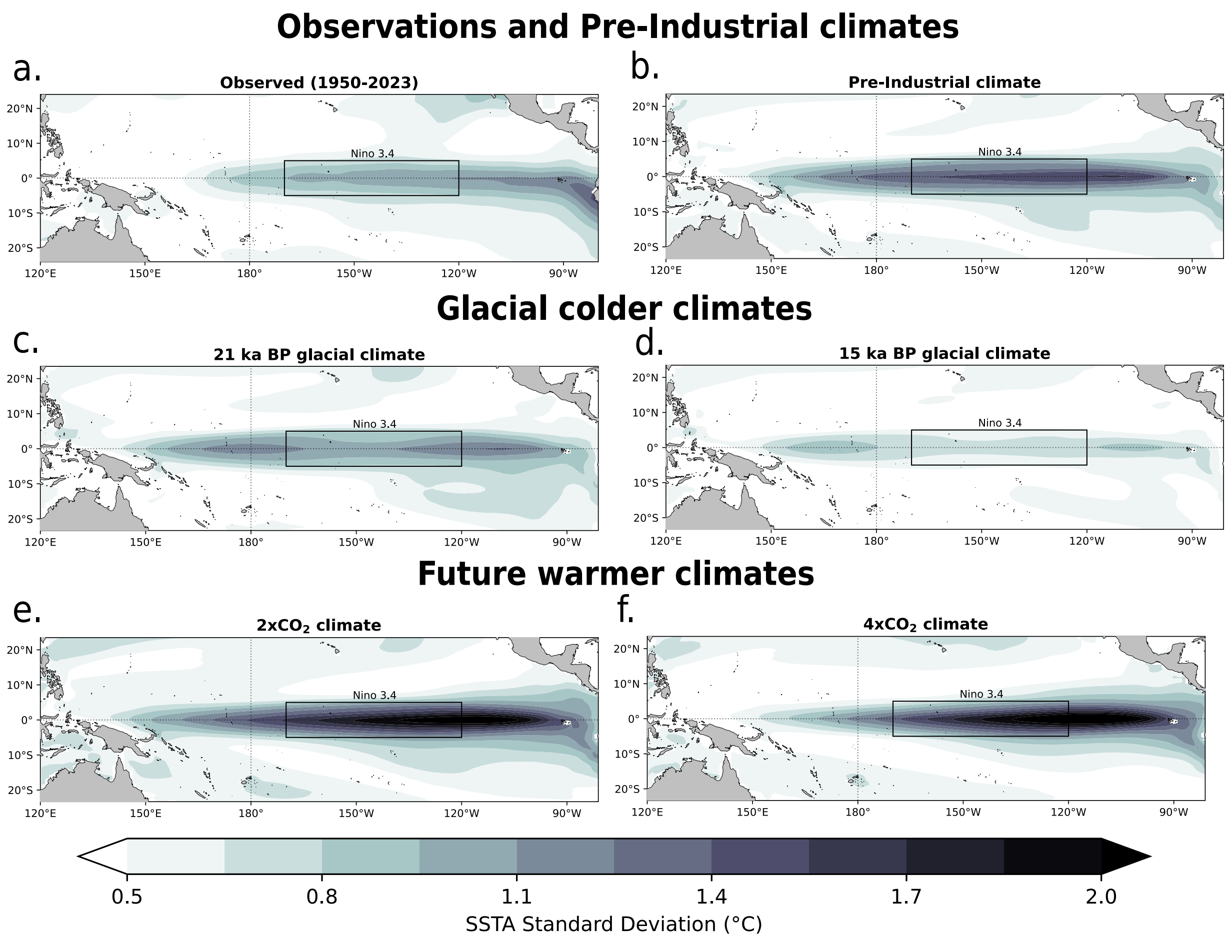

FIG. 2: **Simulated and observed patterns in the anomalous SST variability in altered climate states.**

Patterns of anomalous sea-surface temperature (SST) variability (shading) in altered climate states, as simulated by CESM1, compared with observations. Simulated SST variability is calculated as the standard deviation of monthly SST anomalies in each climate state. The fixed location of the Niño3.4 region (170°W–120°W, 5°S–5°N) is highlighted by the black square.

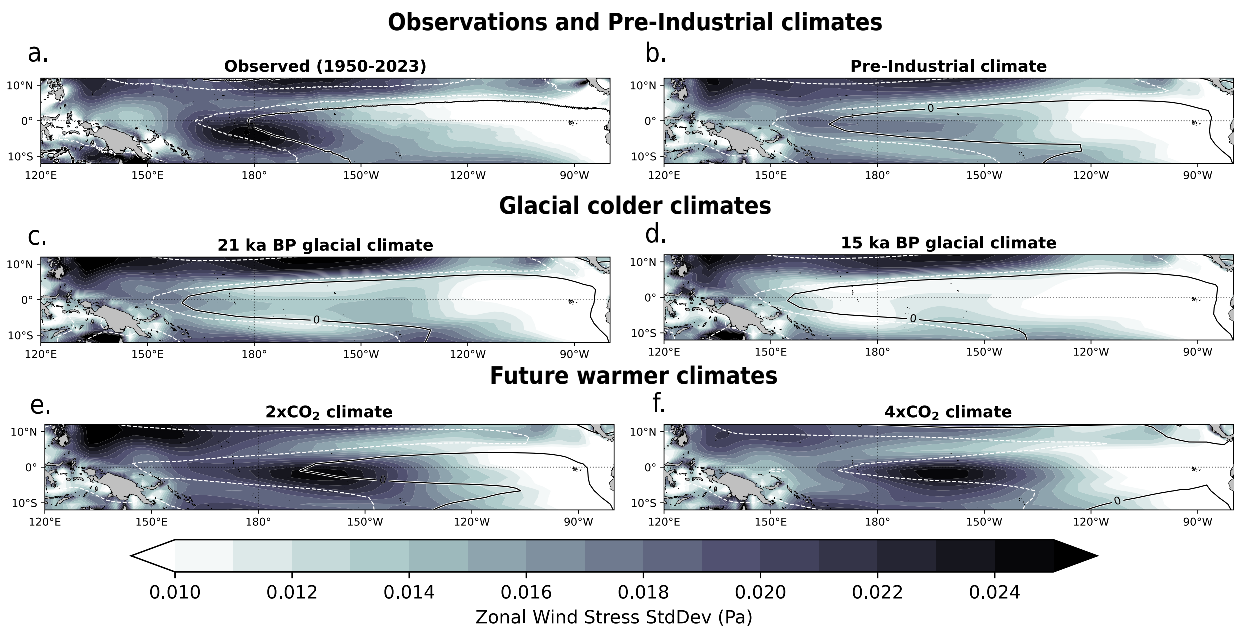

FIG. 3: **Simulated and observed patterns in the anomalous zonal wind stress variability in altered climate states.**

Zonal wind stress variability (shading) in altered climate states, as simulated by CESM1. Variability is calculated as the standard deviation of monthly zonal wind stress anomalies in each climate state. The zero contour of vertical velocity at 500 hPa (black solid conour) is shown to indicate the boundary of the western Pacific warm pool in each climate state. One negative interval of vertical velocity is also shown (white dashed contour) to highlight which side of the Pacific corresponds to upward motion.

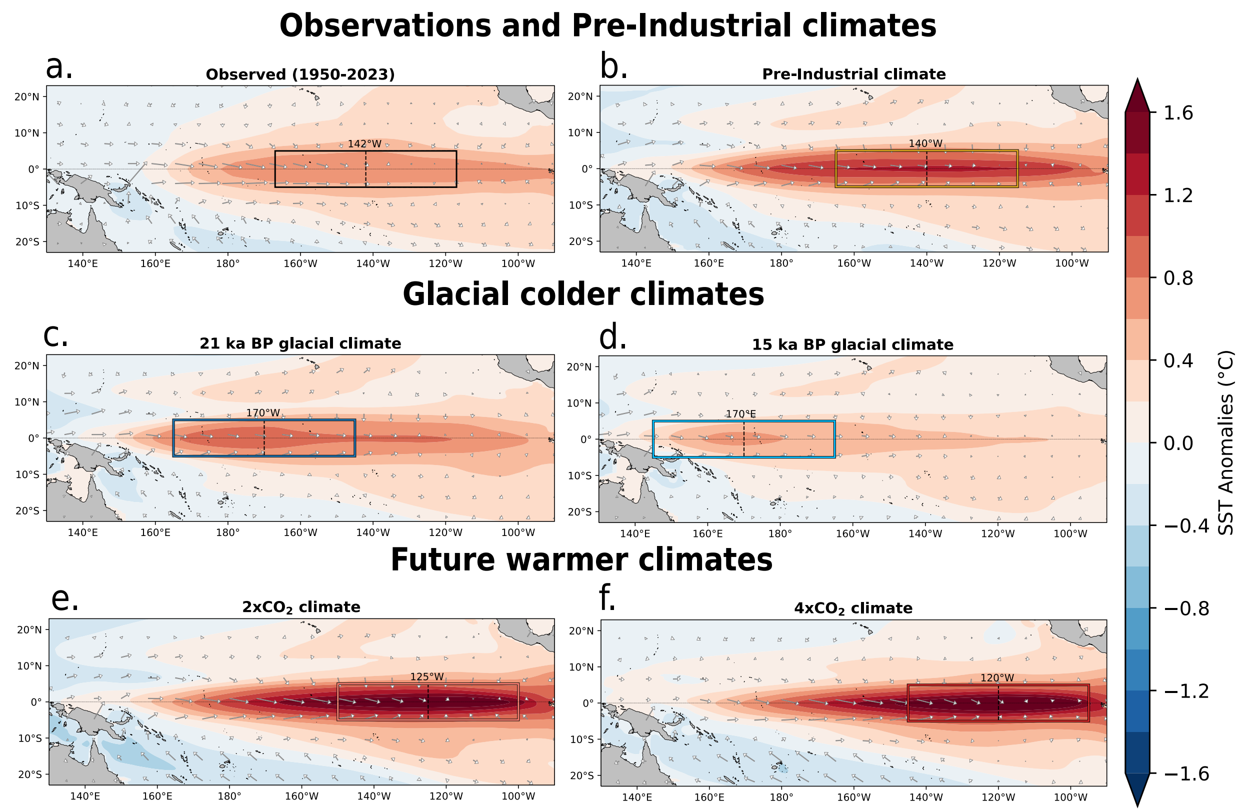

FIG. 4: **Simulated and observed patterns of covariability between SST and zonal wind stress anomalies to identify the ENSO air-sea coupling region.**

Patterns of covariability between SST and zonal wind stress anomalies (shading), as simulated by CESM1 and compared with observations, to identify the ENSO air-sea coupling region. Patterns are derived by regressing SST anomalies onto the first normalized principal component of equatorial zonal wind stress variability (5°S–5°N). The vectors represent the regression values of zonal (τ_x) and meridional (τ_y) wind stress onto τ_x PC1. The coupling region is defined as the area extending 25° east and west of the longitude of maximum equatorial SST regression values (box).

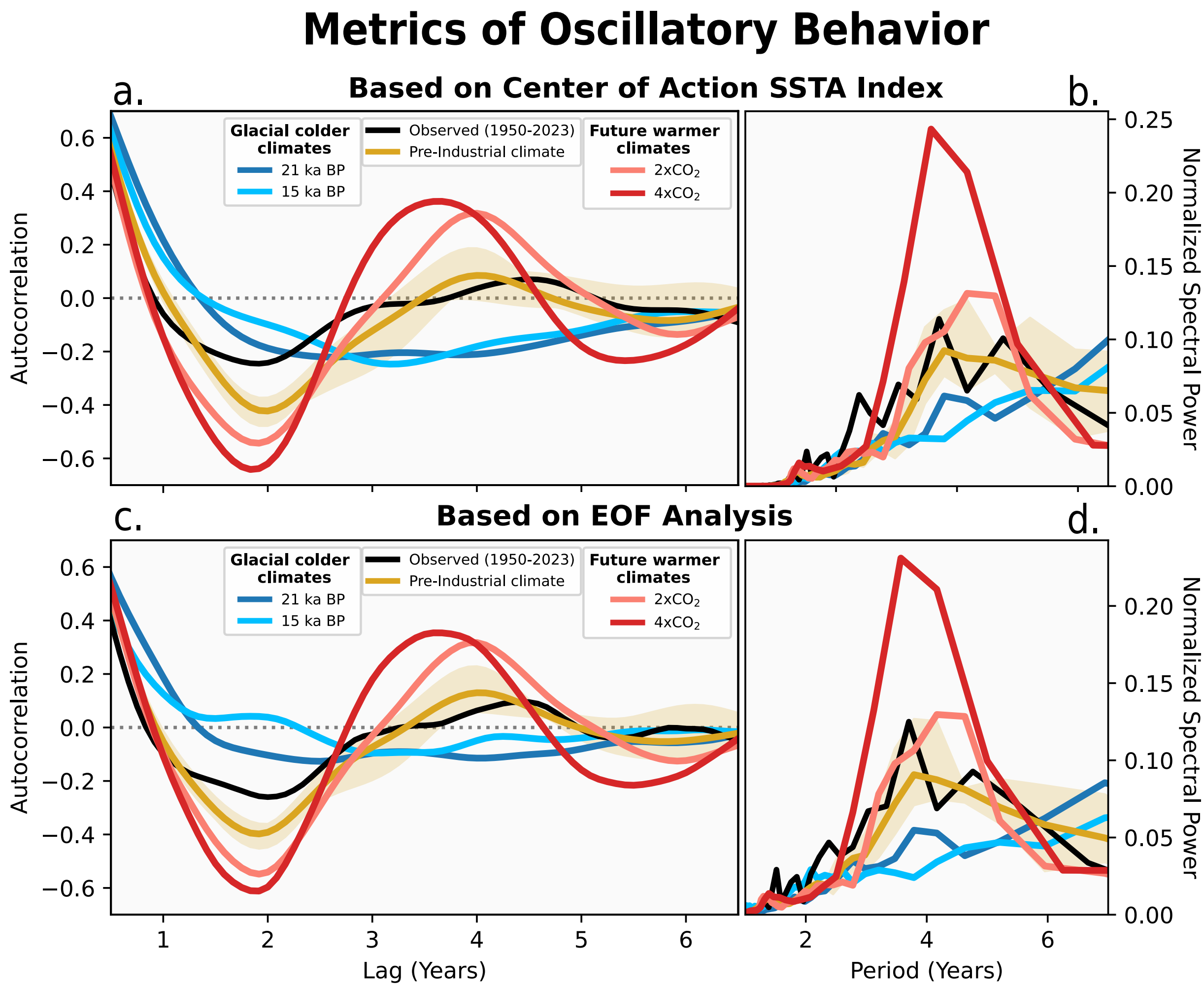

FIG. 5: **Metrics of oscillatory behavior of simulated and observed ENSO variability.**

Metrics of oscillatory behavior in observed and simulated ENSO variability across climate states. (a) Lagged autocorrelation of SST anomalies averaged over the ENSO coupling region. (b) Normalized power spectra of SST anomalies averaged over the Climate-Specific coupling region. (c) Same as (a), but for the first principal component (PC1) of SST anomalies across the tropical Pacific (23°S–23°N). (d) Same as (b), but for PC1 of SST anomalies across the tropical Pacific.

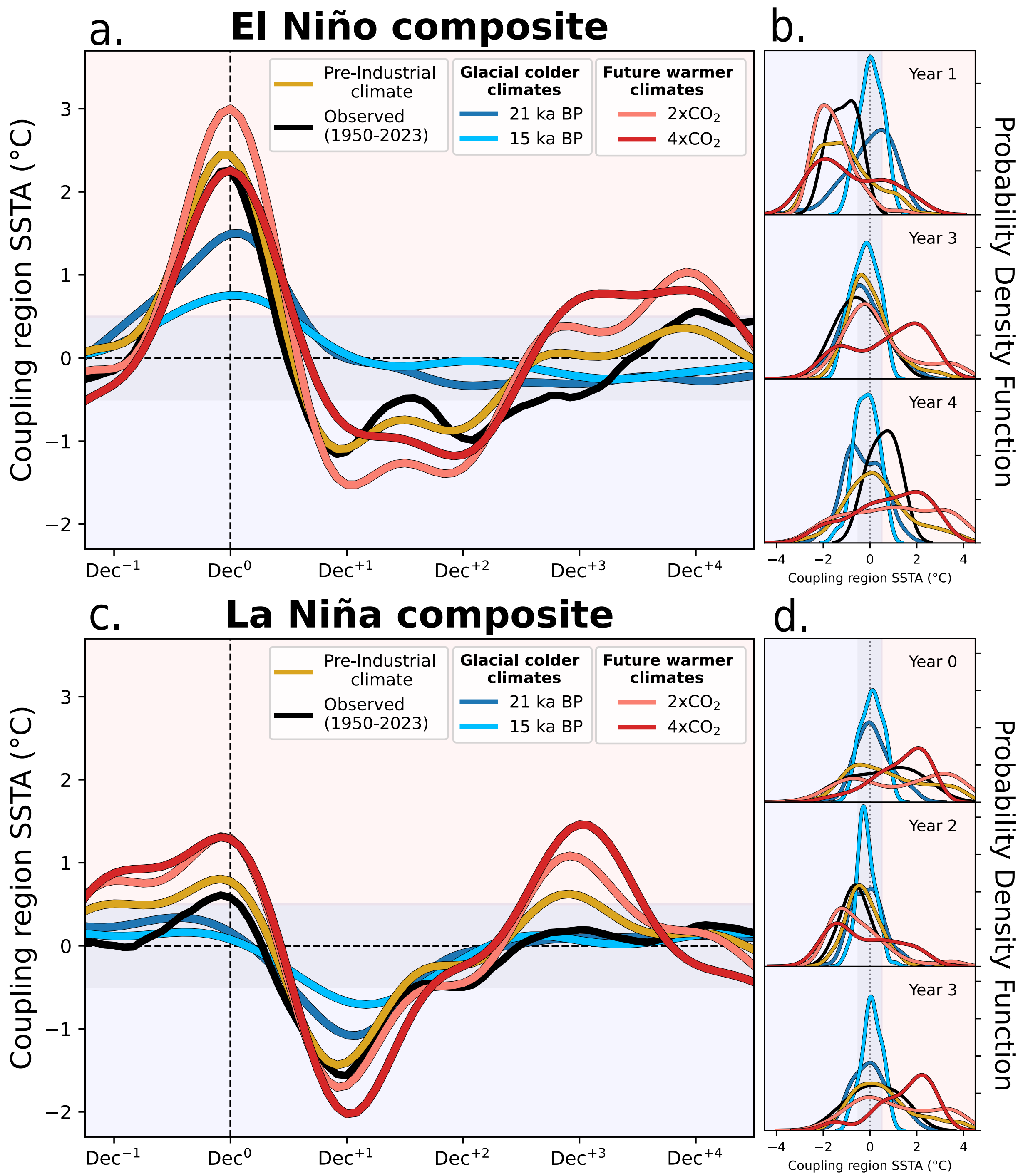

Fig. 6: **Composite evolution of El Niño and La Niña events for the coupling region in each of the altered climate states**

Composite evolution of El Niño and La Niña events based on SST anomalies in the Climate-Specific coupling region, as simulated by CESM1. (a) Composite of El Niño events exceeding a threshold of one standard deviation specific to each climate state, aligned to December, the typical peak month of ENSO in boreal winter. The mean of all events is shown to highlight common behavior, with observations (black solid line) included for comparison with the pre-industrial (PI) simulation. (b) Probability density function showing the distribution of El Niño events at key temporal intervals (years 1, 3, and 4). (c) Same as (a), but for La Niña events, with year 0 aligned to one year before the peak of La Niña events. (d) Same as (b), but for La Niña events at key intervals (years 0, 2, and 3).

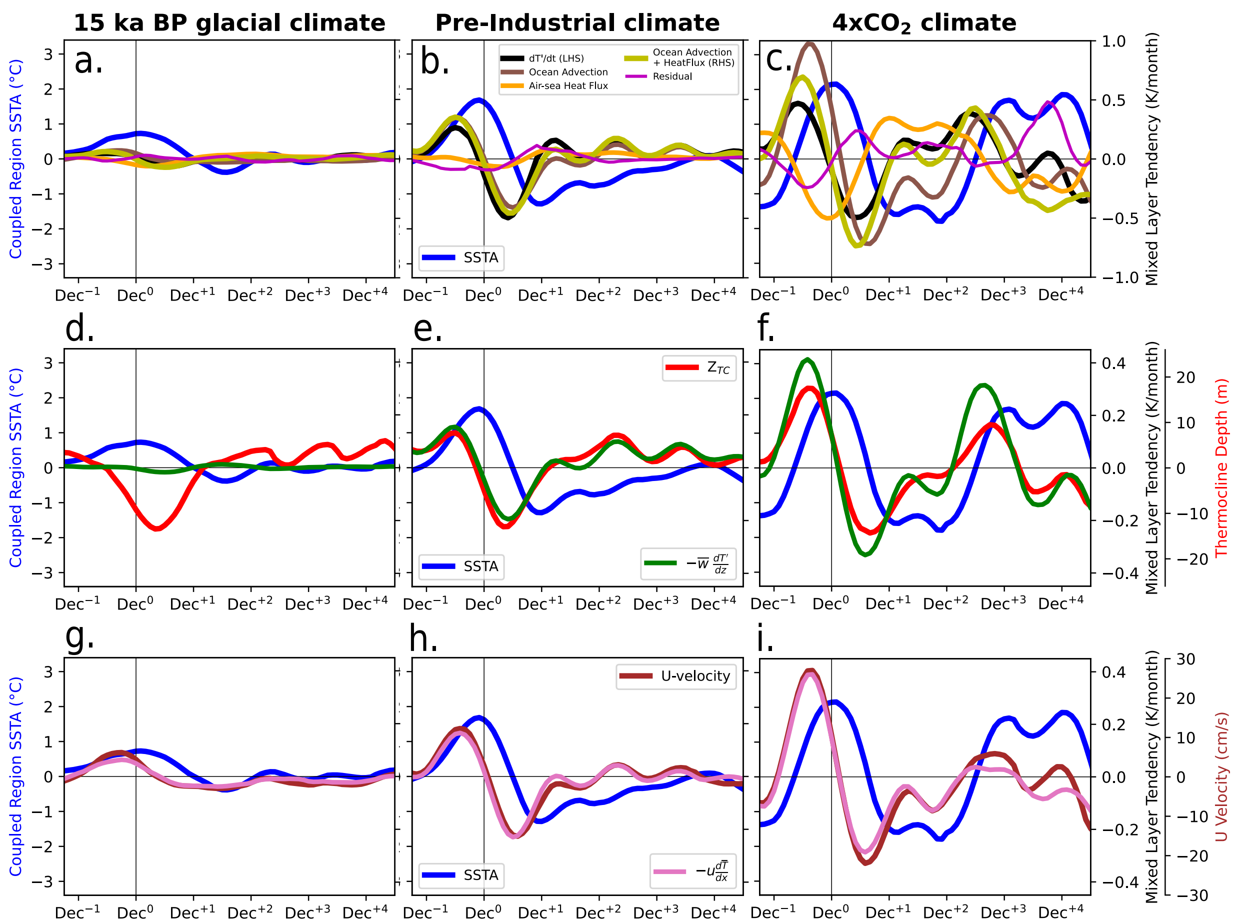

FIG. 7: **Mixed Layer Heat Budget Analysis for each climate state**

Mixed-layer heat budget analysis for El Niño events in each climate state, as simulated by CESM1. Composite heat budget terms are shown during the development, transition, and decay phases of ENSO events, with December of year zero marking the peak of SST anomalies (blue line) in all panels. **Top row**: Heat budget terms include the full tendency (black line), major ocean thermal advection terms (brown line), air-sea heat flux (yellow line), and residual terms (purple line). **Middle row**: The depth of the thermocline (red line) and the vertical thermal advection of anomalous temperature by the mean vertical velocity (green line) are shown, where positive values of the green line indicate a warming tendency and negative values indicate a cooling tendency of the mixed layer. **Bottom row**: Zonal current (purple line) and its associated zonal thermal advection term (pink line) are displayed. All variables are presented as seasonal anomalies averaged over the Climate-Specific coupling region, defined by equatorial latitudes (5°S–5°N) and longitudes listed in Table 2.

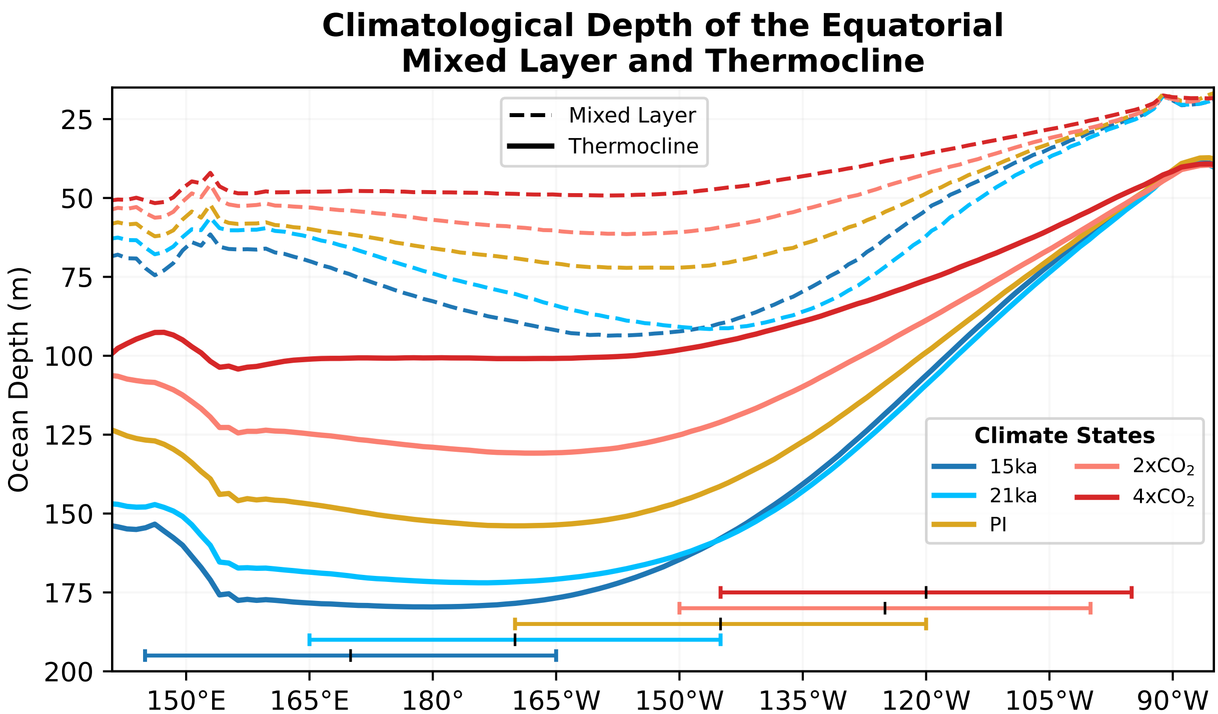

FIG. 8: **Climatological depth of the equatorial mixed layer and thermocline across past and future climate states.**

Climatological depth of the equatorial mixed layer (dashed lines) and thermocline (solid lines) across past and future climate states, as simulated by CESM1. Results are shown for the five climate intervals, with horizontal whisker lines at the bottom of the plot indicating the zonal extent of the coupling region for each climate state. The mean depth of both the mixed layer and thermocline shoal in warmer climates and deepens in colder climates, while the relative separation between the thermocline and the mixed layer remains nearly constant across all climates.

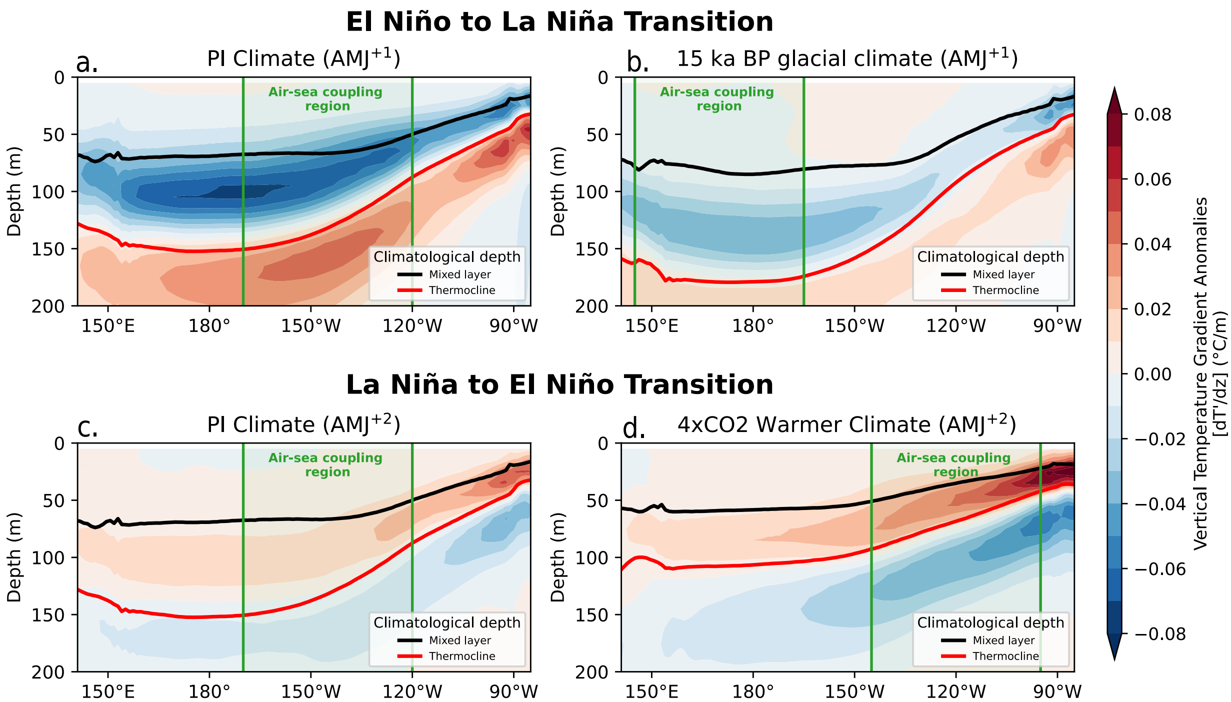

FIG. 9: **Thermocline-mixed layer coupling during the onset of La Niña and El Niño**

Seasonally averaged composites of sub-surface vertical temperature gradient anomaly (shading), mixed layer depth (black contour), and thermocline depth (red contour) during phase transitions of ENSO events. Negative (positive) values of vertical temperature gradient (shading) indicate a more (less) thermally stratified upper ocean. (a) Transition from El Niño to La Niña are shown for the April-May-June (AMJ^{+1}) period, 4-6 months after the peak of El Niño for the PI climate. (b) same as (a) but for the 15 ka BP glacial climate. (c) Transition from La Niña to El Niño are shown for the AMJ^{+2} period, 16-18 months after the peak of La Niña for the PI climate. (b) same as (a) but for the warmer 4xCO_2 climate.

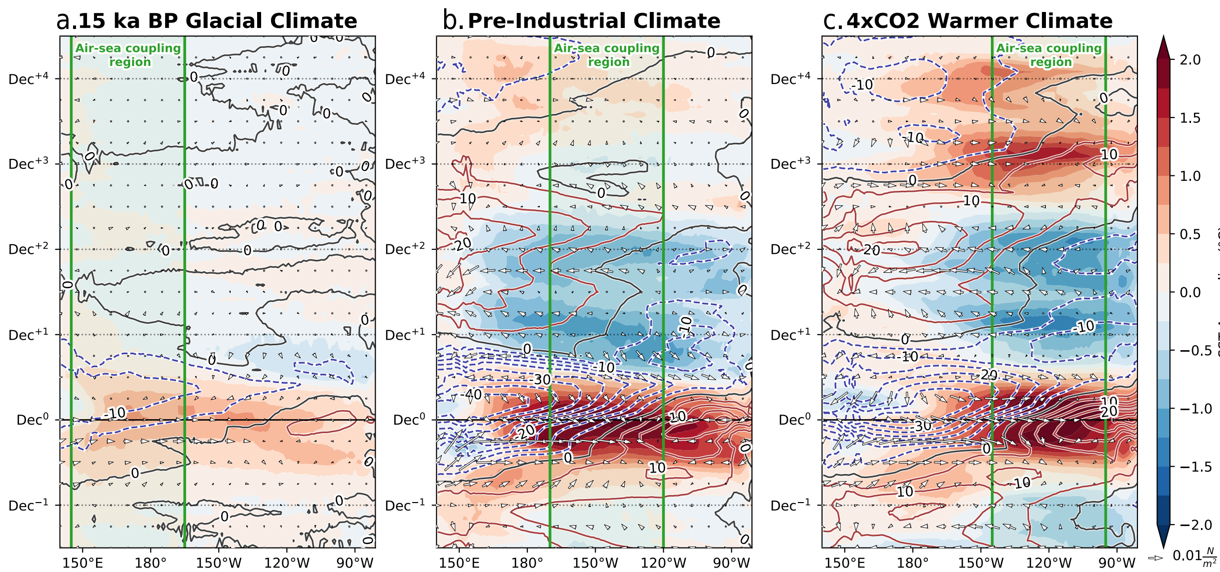

Fig. 10: **Hovmöller plots for El Nino temporal evolution in the 15 ka BP, pre-industrial, and 4xCO2 climates**

Hovmöller plots illustrating the temporal evolution of El Niño events in the 15 ka BP, pre-industrial, and 4xCO_2 climate states, as simulated by CESM1. Longitude–time sections along the equator (5°S–5°N) of SST anomalies (0.25 K intervals, color shading), thermocline depth anomalies (contours, 5 m intervals), and horizontal wind stress anomalies (N m^{-2}, vectors). The analysis focuses on events defined using the Climate-Specific coupling region SST indices for each climate state defined in Table 1.